

Effect of thermal mismatch induced residual stresses on grain boundary microcracking of titanium diboride ceramics

M. Pezzotta · Z. L. Zhang

Received: 5 April 2009 / Accepted: 3 October 2009 / Published online: 20 October 2009
© Springer Science+Business Media, LLC 2009

Abstract The effect of thermal mismatch induced residual stresses on grain boundary microcracking in titanium diboride (TiB_2) ceramics has been studied by finite element method. A cohesive zone model was used to simulate the microcracking initiation in four-point bending specimens. In particular, the microcracking was assumed to occur at a grain boundary which is located in the center of the specimen, surrounded by a thermally anisotropic area. The predicted failure strength appears to be significantly reduced by the presence of residual stresses when the cohesive energy of the microstructure is small. The failure load from experiments has been used to determine the critical damage parameters for microcracking initiation in both pristine and aluminum-infiltrated TiB_2 . A viscous regularization technique is employed in the simulations to improve the rate of convergence of the solution and the effect of the value of the viscosity parameter on the simulation results, has been investigated. The effect of grain size, grain orientation, and number of employed thermally anisotropic grains, on the microcracking is also discussed.

Introduction

Microcracking in titanium diboride (TiB_2) polycrystalline ceramics is not desirable in view of its possible employment as cathode material in the electrolysis process of production of aluminum. Primary source of microcracking in such material are residual stresses which arise during the fabrication process because of the thermal anisotropy at

grain level in combination with cooling from about 1500 °C to room temperature. Moreover, it has been reported that TiB_2 is subjected to grain boundary penetration by liquid aluminum at high temperatures and this leads to further weakening of the material [1–3].

Several studies have focused on the calculation of the residual stress field along grain boundaries which are the most likely location for microcracking nucleation in polycrystalline materials [4–8]. It is well-established that a critical grain size exists and thermal induced microcracking can be avoided in microstructures with grain size smaller than the critical one. Nevertheless, after fabrication and during service the material will be possibly subjected to external load which can create additional stresses along the grain boundary and give rise to brittle fracture. It is important to understand the contribution of the residual stress on the failure strength. In the present paper, finite element (FE) models are employed to investigate the effect of residual stresses on microcracking. Because the material is brittle the load at which a microcrack initiates at the grain boundary located at the center of four-point bending specimens is taken as the failure load. Subsequently, the failure load is normalized and the results are presented as failure strength. In addition, the weakening effect of Al penetration is also investigated by the use of the experimental results of Al-exposed TiB_2 specimens from an early study of the authors [3].

Cohesive zone models available in ABAQUS, whose damage and failure are controlled by a critical traction and a cohesive energy density, have been utilized to model the grain boundary cracking behavior. The cohesive energy density corresponds to the grain boundary energy in this case. In the last decade cohesive elements have been often used to simulate delamination. When modeling thin brittle interfaces by cohesive elements, numerical problems can

M. Pezzotta · Z. L. Zhang (✉)
Department of Structural Engineering, Norwegian University
of Science and Technology (NTNU), 7491 Trondheim, Norway
e-mail: zhiliang.zhang@ntnu.no

arise in quasi-static simulations [9–11]. Different solutions are proposed in the literature, such as mesh refinement, viscous regularization, and the use of a local arc-length control procedure [11–13]. The viscous regularization method is used in the present study.

The paper is organized as follows. In the first section, a description of the employed FE model, the material properties, and the viscous regularization technique used is given. Then the main numerical results are presented and the effect of the chief parameters on the failure strength by brittle fracture is discussed. Experimental data for both pristine and Al-infiltrated TiB₂ from Ref. [3] were used to extract the corresponding critical grain boundary energy density. Lastly, some conclusions are drawn.

FE model, material data, and regularization technique

The dimensions of the 4-point bending specimen are shown in Fig. 1. The width of the specimen is 4 mm. A two-dimensional FE model of the specimen with about 40000 elements was created. Plane strain four-node elements were employed. In order to take into account thermal anisotropy-induced residual stresses, the microstructure model is based on Clarke’s model [7]: two grains surrounded by matrix material are used and the grain shape is square (Fig. 2). The grain dimension *l* is 10 μm, slightly larger than the one of the material studied in the experimental work by Jensen et al. [3]. Grain sizes of 20 and 50 μm were also considered in order to investigate the grain size effect. The grain area is located at the origin of the model, Fig. 2. A 2-grain ensemble with grains symmetric to the *x*-axis is taken as the basis for the study. For comparison purpose 8-grain and 72-grain ensembles were also considered. The TiB₂ material has Young’s modulus 732 GPa at room temperature [3], and Poisson’s ratio 0.108 from literature [14]. As in Clarke’s work [7], the material surrounding the grains,

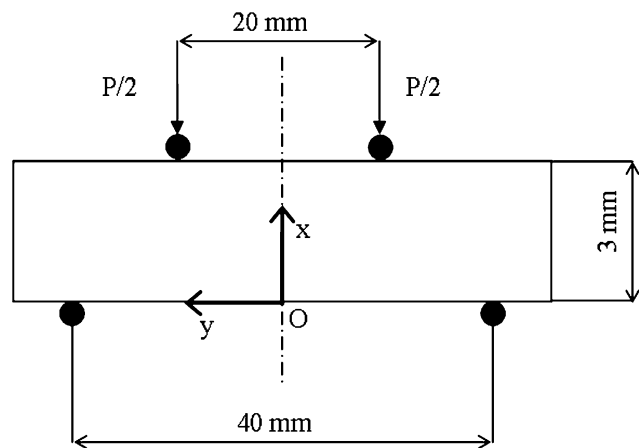


Fig. 1 Four-point bending setup

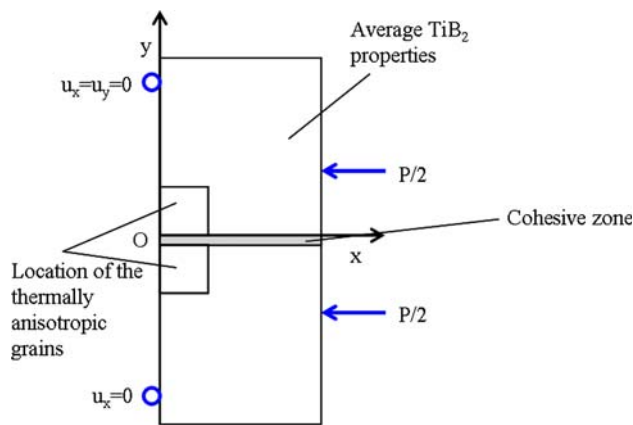


Fig. 2 Specimen’s model: the grains, the cohesive zone, and the boundary conditions are indicated in the sketch; the dimensions of the cohesive zone and of the grains are exaggerated for clarity

previously called matrix material, is assumed thermally isotropic with TiB₂’s average properties (Fig. 2); each grain is thermally anisotropic with thermal expansion coefficients being dependent on the crystallographic directions. Thermal expansion coefficients, denoted by α_i , are taken from Ref. [14]; they are increasing functions of the temperature and their values are of the order of 10⁻⁶ K⁻¹. The angle between the direction of maximum thermal expansion and the *x*-axis is denoted by θ , Fig. 3. The default angle θ is equal to 45° when not otherwise specified. Elastic isotropy is assumed everywhere.

The specimen is subjected to a thermal and a mechanical load. The simulations consist of two load-steps: the first is the application of a change of temperature corresponding to a cooling process. The production of ceramics by sintering or hot-pressing is carried out at high temperatures. Therefore, the final stage of fabrication of ceramics cools down from high temperatures to room temperature. The initial temperature is chosen here as 1500 °C and the final one is

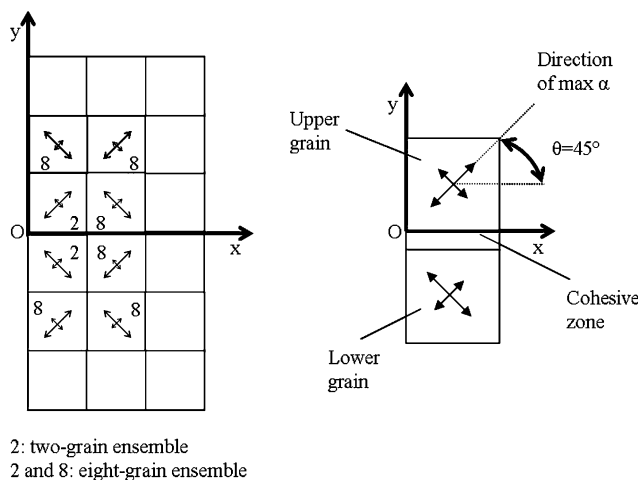


Fig. 3 Schematic plots of the grain ensembles

20 °C. The second step is the enforcement of the mechanical loading on the specimen according to the 4-point bending setup (Fig. 1).

The failure load was measured by 4-point bending test and is about 579 N at room temperature for the pristine material. The corresponding failure strength is about 483 MPa. For TiB₂ material exposed to liquid aluminum for 1.5, 2, and 3 h, the penetration depths were 0.2, 0.45, and 0.65 mm, respectively. The details can be seen in Ref. [3]. The Young’s moduli for the Al-infiltrated samples are 587, 576, and 563 GPa at room temperature, respectively [3].

The grain boundary of interest is modeled by a long sequence of cohesive elements in the middle of the model (at $y = 0$), with initial thickness $T_0 = 1.0E-5 \mu\text{m}$. The length of the cohesive elements close to the origin is 2.5 μm ; the length increases up to 10 μm for the elements along the x -axis direction within the distance 50–1000 μm from the origin O and to a maximum of about 20 μm (Fig. 4). The stiffness of the interface, K_{int} , is of the order of 10^{12} N/mm^3 . A bilinear traction–separation law is employed to describe the behavior of the interface, i.e., the grain boundary (Fig. 5). The material response is linear elastic up to the critical traction. After the critical traction is reached, the process zone starts to develop and the material stiffness is degraded. From this point, the normal traction is a decreasing linear function of the opening distance between the upper and lower surfaces of the cohesive elements.

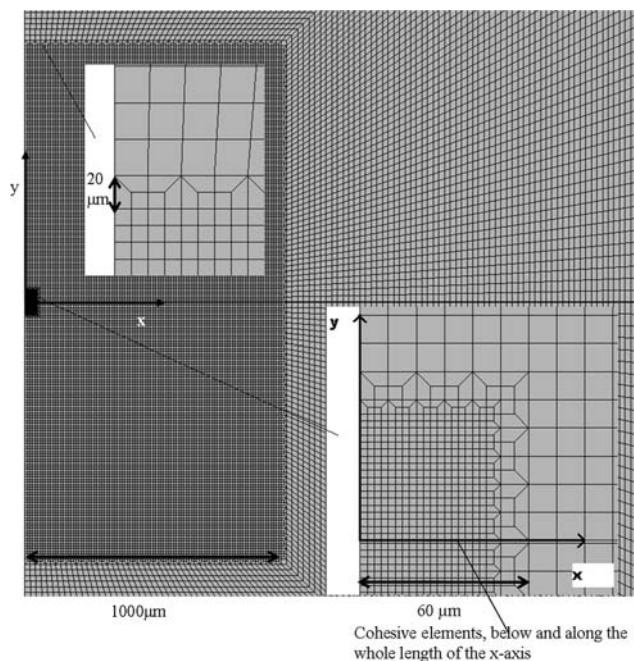


Fig. 4 FE model: global and local mesh

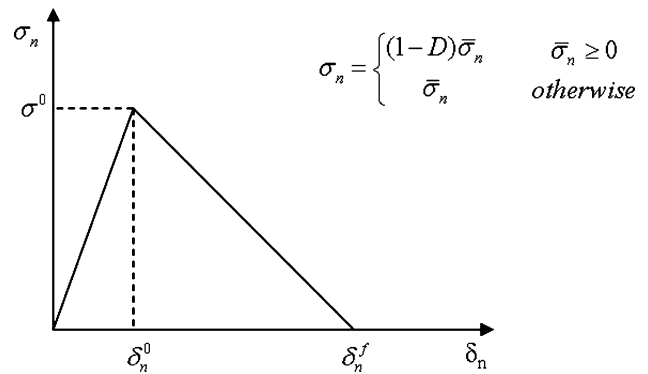


Fig. 5 Bilinear traction–separation law without viscosity regularization: normal component of traction and normal opening displacement/separation

The critical traction σ^0 , which determines the beginning of the damage process, is chosen as 800 MPa. Other values were also employed (900 and 1000 MPa) and a discussion about the effect on the results is reported in the next sections. The interface constitutive behavior is given by:

$$\sigma_n = (1 - D)K_{\text{int}}\delta_n$$

with σ_n the normal traction, δ_n the opening displacement between the two crack surfaces, and D the damage variable (Fig. 5). D has values belonging to the range 0–1, where $D = 0$ is the initial value, when no damage has developed. In the present study, a linear softening law was chosen to describe the damage evolution of the interface after the critical traction is reached; the damage variable progresses according to the following law [15]:

$$D = \frac{\delta_n^f (\delta_n^{\text{max}} - \delta_n^0)}{\delta_n^{\text{max}} (\delta_n^f - \delta_n^0)} \quad \text{with } \delta_n^f = \frac{2G_c}{\sigma_{\text{eff}}^0}$$

where σ_{eff}^0 is the effective traction at damage initiation and δ_n^{max} the maximum value of the effective displacement attained during the loading history. Note that all the quantities here refer to the normal component of the corresponding variable because in the present study only the normal component is considered.

In the present simulations the use of a regularization technique was necessary in order to complete the calculations. More details about the nature of the instability are discussed in the next section. The viscous regularization available in ABAQUS was employed. The value of viscosity $\nu = 1.0E-5$ was used in the analyses. In addition, a study of the effect of the viscosity value on the failure strength was carried out and results are presented in the next section. Briefly, the viscous regularization of the cohesive elements’ constitutive equation consists in the introduction of a viscous stiffness degradation variable D_ν . The evolution of the variable D_ν is described by the following equation [15]:

Table 1 Summary of the parameters employed in the present study

Type of parameter	Parameter	Symbol	Value (other values)	Source
Specimen dimensions	Length		50 mm	Experimental
	Width		4 mm	Experimental
	Thickness		3 mm	Experimental
Material properties	Elastic	E ($T = 20\text{ }^\circ\text{C}$)	732 GPa	Experimental
		ν	0.108	Literature [14]
	Thermal	α_i	$6 \div 11 \times 10^{-6}\text{ K}^{-1}$	Literature [14]
	Grain orientation	θ	45° (0° ; 90°)	
	Grain size	l	10 μm (20 μm ; 50 μm)	
	No. of grains	n	2 (8; 72)	
Cohesive model	Mesh dimension	Min–max cohesive elements' length (x-direction)	2.5 \div 10 μm	
	Initial thickness	T_0 (y-direction)	1.0E–5 μm	
	Cohesive traction	σ^0	800 MPa (900 MPa; 1000 MPa)	
	Cohesive energy density	G_c	0.03 \div 0.24 N/mm (2 N/mm; 4 N/mm)	
Viscous regularization	Interface stiffness	K_{int}	Order of 10^{12} N/mm^3	
	Viscosity parameter	ν	1.0E–5 (1.0E–9 \div 1.0E–3)	
Cooling process parameters	Initial temperature	T_{in}	1500 $^\circ\text{C}$	
	Final temperature	T_{fin}	20 $^\circ\text{C}$	
Four-point bending parameters	Failure load (pristine material)/corresponding failure strength	$P_{a=0}/\sigma_{a=0}$	579 N/483 MPa	Experimental [3]
Exposure to liquid Al parameters	Exposure time	t	1.5 h 2 h 3 h	Experimental [3]
	Penetration depth	a	0.2 mm 0.45 mm 0.65 mm	Experimental [3]
	Young's modulus	E_a ($T = 20\text{ }^\circ\text{C}$)	587 GPa 576 GPa 563 GPa	Experimental [3]

$$\dot{D}_v = \frac{1}{\nu}(D - D_v)$$

where ν denotes the viscosity parameter. The response of the interface material becomes rate-dependent and is modified as:

$$\sigma = (1 - D_v)\bar{\sigma}$$

where σ indicates the nominal traction stress tensor and $\bar{\sigma}$ represents the stress tensor predicted by the elastic traction–separation behavior for the current strains without damage. Small values of ν improve the rate of convergence of the model without affecting significantly the results [15].

For clarity, the parameters used in the paper are summarized in Table 1.

Results and discussion

The presence of local residual stresses (rs) has a strong effect on the macroscopic failure strength. In the following, the effect of important factors which affects the residual

stresses, such as grain orientation, grain size, and number of grains has been studied and results are presented. The parameters employed to simulate damage and fracture (G_c , σ^0 , and K_{int}), and the viscosity parameter (ν), are linked to the material properties but have also an important role from the numerical point of view as it will be shown in the following.

Effect of viscosity parameter

When cohesive elements are employed to simulate the cracking behavior of a brittle thin interface, the softening part of the cohesive law can cause some problems to the solution algorithm. A snap-back instability can occur depending on geometry (interface thickness T_0), interface behavior (interface stiffness K_{int}), and FE discretization (length of the elements adjacent to the cohesive zone) [11]. If a discontinuity of the response occurs, the simulation can stop. More details of the problem can be found in references [11–13]. A possible solution is the viscous regularization method [11]; this consists in introducing a fictitious

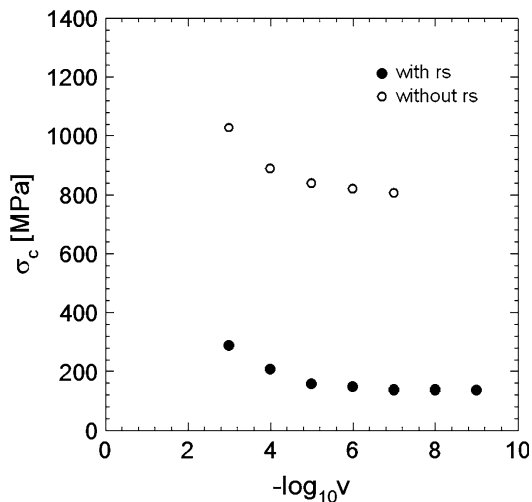


Fig. 6 Effect of viscosity values ν ($G_c = 0.01$ N/mm)

viscosity parameter in the constitutive equation of the cohesive elements. Its effect is to help the convergence of the solution by dissipating excess energy; but the value of the viscosity parameter should be small enough to not affect the results [12]. The effect of the viscosity parameter on the simulated failure strength σ_c is presented first (Fig. 6). It can be seen that for values $\nu \leq 1.0E-5$ the predicted σ_c becomes independent of the viscosity parameter. A large value of viscosity corresponds to an overestimation of the failure strength for both cases with and without residual stresses. If a value of ν significantly smaller than the characteristic simulation increment size is used, the analysis terminates just after the critical traction for damage initiation σ^0 , is reached at the first cohesive elements/nodes along the grain boundary. It was also found that the convergence of the model without residual stresses is more difficult than the case with residual stresses, probably because of the more homogeneous stress field in the cohesive elements. The viscosity parameter's value was chosen as the minimum one which could guarantee convergence in all cases, namely for different combination of grain size, cohesive energy density, and load. Even though in some particular cases a smaller value could be used, all the results presented below were calculated using the same $\nu = 1.0E-5$, in order to keep consistency.

Effect of residual stresses

In Fig. 7 the predicted failure strength is plotted as a function of the cohesive energy density. When the cohesive energy density G_c is smaller than 0.1 N/mm, the failure strength without residual stresses is close to 1000 N. The results in Fig. 7 show that residual stresses weaken strongly the strength of the material. This difference of failure strength is more pronounced at small cohesive

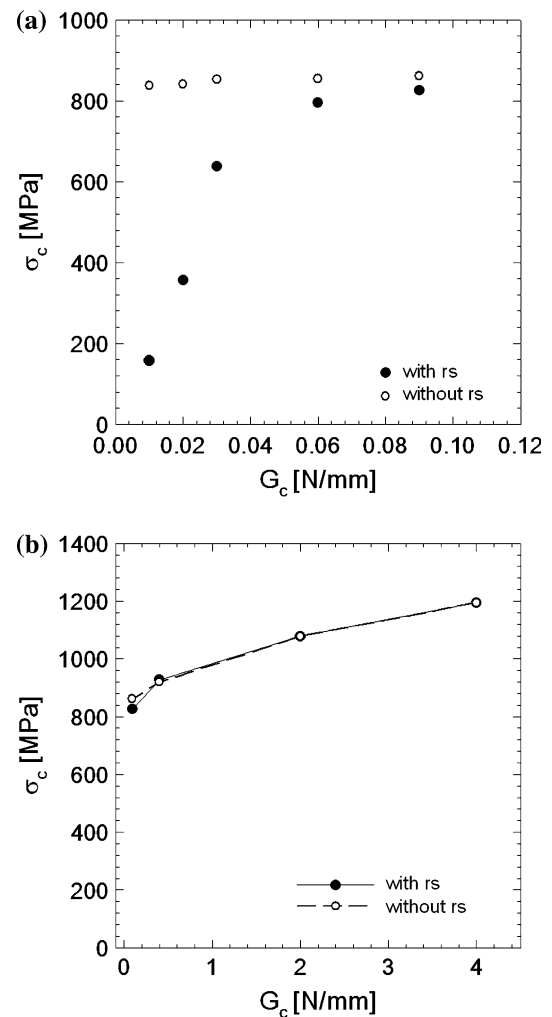


Fig. 7 Residual stresses effect on the failure strength: **a** small cohesive energy densities; **b** large cohesive energy densities

energy density levels (Fig. 7a). Residual stresses are local stresses which have a large effect on the formation of microcracking. The failure strength for the case with residual stresses shows a stronger dependence on the cohesive energy density. It can be expected, as shown in Fig. 7b, that when the cohesive energy G_c is large enough (larger than 0.4 N/mm) in the present case, the effect of the residual stresses can be neglected. This is due to the fact that when the grain boundaries possess a cohesive energy which exceeds a critical value, the material has such a strong microstructure that the effect of local residual stresses becomes negligible with respect to the strain energy necessary to break the grain boundary.

Effect of grain size

Grain size plays an important role in microcracking. In addition to the case with grain size 10 μm , two models with grain size 20 and 50 μm have been created. A

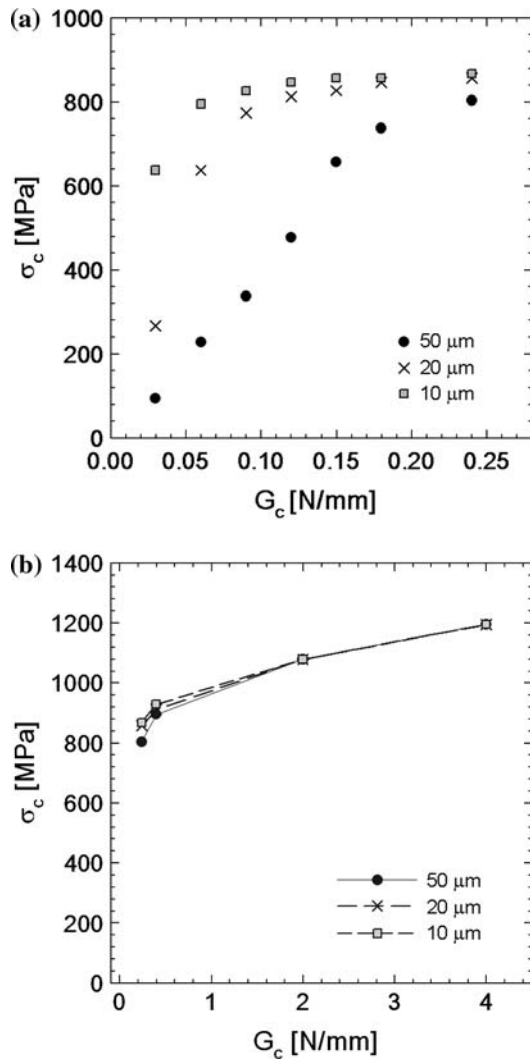


Fig. 8 Grain size effect on the failure strength for the case with residual stresses: **a** small cohesive energy densities; **b** large cohesive energy densities

microstructure with smaller grains is expected to have stronger cracking resistance. In Fig. 8 the failure strengths for different grain size microstructures are plotted as a function of cohesive energy density. It is interesting to note that for $G_c = 0.03$ N/mm the failure strength for grain size 10 μm is about 6 times that for the case with 50 μm . The failure strength for the case with residual stresses approaches to the one without residual stresses as the cohesive energy density increases. The failure strength as function of cohesive energy density shows a linear trend for small cohesive energy densities.

Effect of grain orientation

Material orientation also affects the residual stress distribution and further the failure strength. Three cases with

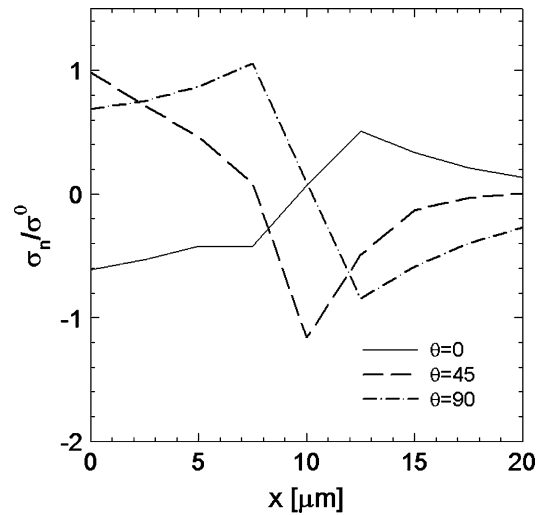


Fig. 9 Effect of grain orientation on the residual stress distribution along the grain boundary ($G_c = 0.01$ N/mm)

same grain size 10 μm but different angles, $\theta = 0^\circ$, 45° , and 90° , were considered (see Fig. 3). In Fig. 9 the opening stress distribution along the grain boundary in the model with two grains is plotted after the cooling process is completed (at room temperature). It results from this analysis that the stress distribution for the case $\theta = 0^\circ$ is the least favorable for microcracking. In fact the opening stress resulting from thermal anisotropy is compressive in the first 10- μm distance along the grain boundary.

When the grain orientation is $\theta = 90^\circ$, the grain boundary is perpendicular to the maximum thermal expansion direction, hence it is expected to experience the largest tensile stress [4]. A large tensile stress means that there is a chance to reach the critical cohesive stress and that damage will start in the grain boundary. In fact the stress distribution shows that damage has already started in the first 7 μm of the grain boundary after the cooling, due to thermal anisotropy (Fig. 9). It is found that in the case $\theta = 90^\circ$ fracture occurs at a lower load, and accordingly shows lower failure strength, than for either $\theta = 0^\circ$ or 45° (Fig. 10).

Effect of number of grains

The number of thermally anisotropic grains included in the model affects the stress distribution, hence the microcracking initiation, as previously observed by Evans [4]. Three cases, 2-, 8- and 72-grain ensembles, were considered with grain orientation $\theta = 45^\circ$ (Fig. 4).

The results in Fig. 11 show that the model with 72 grains predicts the lowest failure strength. It is interesting to note that the failure strength does not show a regular trend as the number of grains changes: the failure strength by the 2 grains model falls between the cases 8 and 72 grains when the

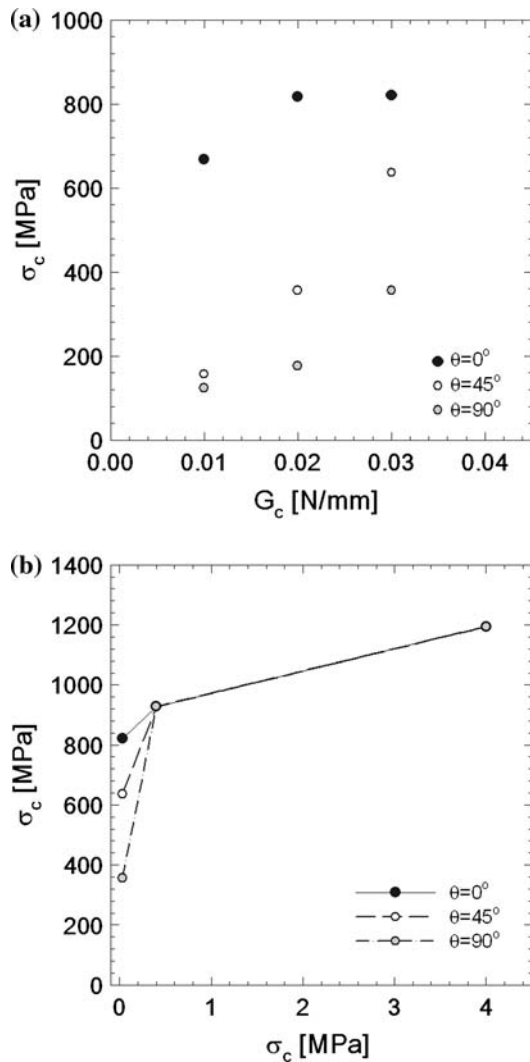


Fig. 10 Grain orientation effect: **a** small cohesive energy densities; **b** large cohesive energy densities

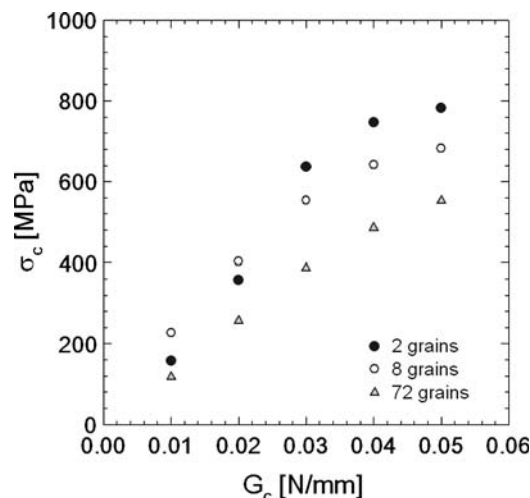


Fig. 11 Effect of number of grains on the failure strength with grain orientation $\theta = 45^\circ$

cohesive energy density is small. The exact reason is not very clear to the authors. Probably due to the free boundary on the y axis (Fig. 4) the 2- and 8-grain model are not consistent to each other. For larger cohesive energy densities ($G_c \geq 0.03$ N/mm), a systematic trend can be observed—increasing the number of grains reduces the failure strength. The increased constraints given by the presence of neighboring and pre-stressed grains can explain the lower failure strength for the model with larger number of grains.

Effect of damage parameters

The failure strength increases with the increase of G_c . In Fig. 7 the failure strength is depicted as a function of cohesive energy density. The experimental failure load measured in 4-point bending tests [3], or equivalently the failure strength, can be used to find the corresponding cohesive energy density predicted by the 2-grain model with $\theta = 45^\circ$ and $\sigma^0 = 800$ MPa. The experimental failure load of pristine TiB₂ which is 579 N (failure strength 483 MPa), corresponds to a cohesive energy density approximately equal to 0.025 N/mm (Fig. 7).

The value of the critical traction should be chosen in connection with the interface material properties [10]. In the present case no experimental measurements were available. The material displays average macroscopic flexural strength 411 ± 152 MPa. With a value of critical traction (or interface strength) equal to 1000 MPa, the simulations had problems of convergence in some cases. Lower values of critical traction can improve the computational burden but too low values can affect extensively the accuracy of the results [9, 10]. Therefore, the effect of the value of σ^0 on the failure strength was studied. Figure 12 shows that when a smaller value of σ^0 is used,

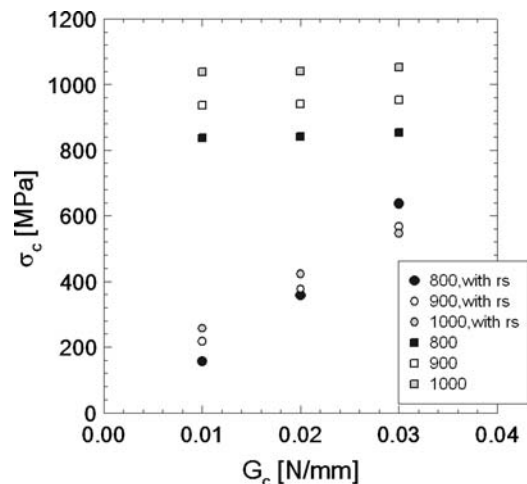


Fig. 12 Effect of critical traction σ^0 on failure strength σ_c , in the cases with and without residual stresses (rs). The numbers indicate the value of σ^0 in MPa

the failure strength predicted by FE calculations is smaller but still in a fairly acceptable range. Particularly, in the case with residual stresses the effect of σ^0 is almost negligible. In light of these results, the critical traction was assumed equal to 800 MPa which is a reasonable compromise between the two issues. The value of the critical traction has also an effect on the results in connection with the used mesh refinement level. A large value of the critical traction can cause spurious oscillations of the global response [10]. Turon et al. [9] proposed a method to determine the value of the necessary critical traction to obtain satisfactory results given the mesh size. In the present case this effect was not observed, thus the parameters chosen seem to be appropriate to the mesh refinement level.

In Fig. 12 a slight irregularity in the trend of the failure strength as function of the cohesive energy for different critical tractions can be observed at $G_c = 0.03$ N/mm for the case with residual stresses. It should be pointed out that the failure strength's values reported are calculated from the failure loads which are average ones between the loads at which the stress field changes from positive to zero at the first nodes along the grain boundary. Hence the irregularity in Fig. 13 can probably be caused by the numerical procedure.

The values of the process zone corresponding to different G_c are reported in Table 2. The length of the process zone as defined by Hilleborg [16], is given by $\frac{EG_c}{(\sigma^0)^2}$. As the cohesive energy increases, the length of the process zone also increases up to a value larger than the length of the specimen thickness. This implies that the problem is in a strength-controlled regime. This is also confirmed by the results in Fig. 12: the resultant failure strength for a given value of G_c , varies for different values of σ^0 .

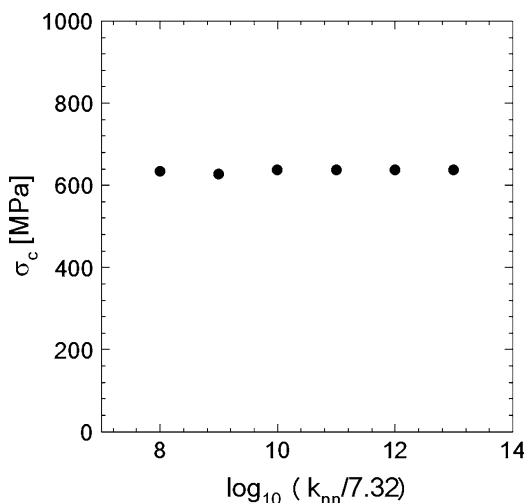


Fig. 13 Effect of the interface stiffness K_{int} on the failure strength σ_c ($G_c = 0.03$ N/mm)

Table 2 Length-scales involved in the present study

Part	Length measured along the x -direction (μm)	
Specimen	3000	
Grain	10	
Cohesive elements	2.5 (for $x = 0\text{--}50 \mu\text{m}$)	
	2.5–10 (for $x = 50\text{--}1000 \mu\text{m}$)	
	10–20 (for $x = 1000\text{--}3000 \mu\text{m}$)	
Cohesive zone	3000	
G_c and corresponding process zone length	G_c (N/mm)	l_{pz} (μm)
	0.01	11.43
	0.03	34.31
	0.24	274.5
	4	4575

The process zone in brittle materials is the damage zone behind the crack-tip where microcracking and crack-bridging activities are present [17]. Depending on the size of the process zone relative to the size of the specimen, the fracture can be in the strength-controlled or in the toughness-controlled regime. The fracture process zone is usually relatively large in small specimens therefore the fracture is dominated by the strength criterion. On the contrary, in large specimens the fracture is controlled by the fracture toughness criterion because the fracture process zone length is relatively small compared to the specimen dimension and to its distance to the nearest specimen boundary. The present case could be comparable to the un-notched case; more detail can be found in [17].

The interface stiffness K_{int} effect was also analyzed. The interface stiffness is a penalty stiffness: its purpose is to guarantee a proper stiffness to the interface without affecting significantly the failure process [9, 10]. A large value of the interface stiffness is necessary to assure a correct representation of the behavior before cracking but too large values can cause numerical problems [9, 10]. The effect of K_{int} on the failure strength is presented in Fig. 13 for the case with residual stresses: for values of K_{int} in the range $7.32\text{E}+8\text{--}7.32\text{E}+13$ N/mm³, the failure strength is about 630 MPa for $G_c = 0.03$ N/mm. With values beyond the indicated range (Fig. 13), numerical problems occurred.

Degraded material

In our previous work [3], four-point bending specimens of TiB₂ were exposed to liquid aluminum at 1000 °C. For different exposure times to liquid Al, different penetration depths a , were measured [3], as summarized in Table 1. Specimens of pristine and Al-penetrated TiB₂ were also subjected to mechanical testing, microindentation, and 4-point bending. In particular, the specimens more extensively penetrated along grain boundaries by liquid Al,

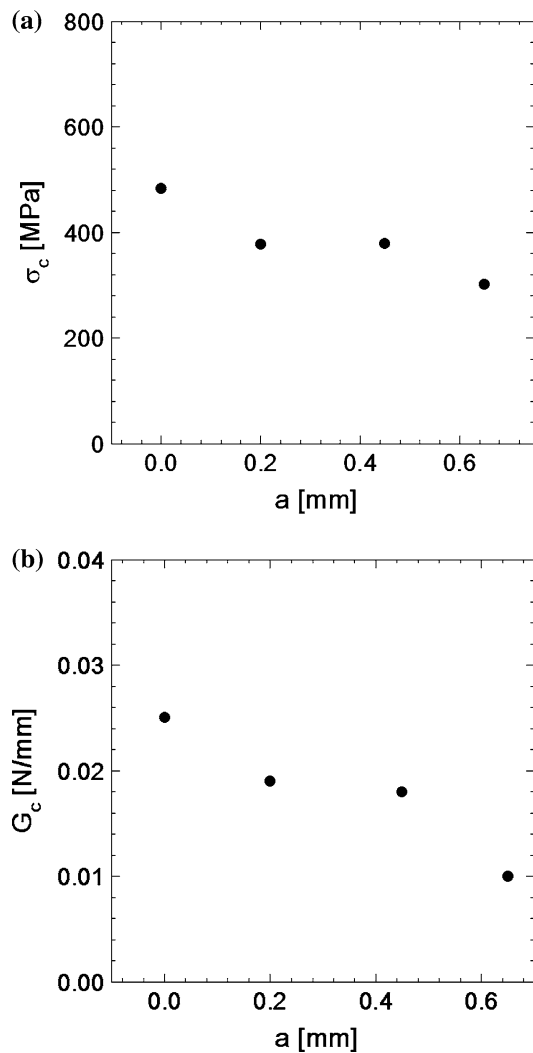


Fig. 14 Experimental failure strength and corresponding cohesive energy density

displayed smaller failure strength (Fig. 14a). The experimental failure load for each level of penetration (the corresponding values of failure strength are reported in Fig. 14a) was used in the present model to find the corresponding cohesive energy for which crack begins at the grain boundary (Fig. 14b). The values were calculated using the 2-grain model, with grain size $10\ \mu\text{m}$ and critical traction $\sigma^0 = 800\ \text{MPa}$. The elastic modulus was also changed according to the experimental values for the materials with different penetration (due to different amounts of exposure time). The simulations show that the grain boundary cohesive energy decreases as the Al penetration depth increases. The specimen penetrated by liquid Al along $0.65\ \text{mm}$ showed a failure load of about $362\ \text{N}$ (failure strength $300\ \text{MPa}$); this corresponds approximately to cohesive energy density $0.01\ \text{N/mm}$ which is less than half the value found for pristine TiB_2 ($G_c = 0.025\ \text{N/mm}$). Therefore, the effect of the liquid Al is to weaken the grain

boundaries such that microcracking occurs more easily. We also observed that the fracture mode in TiB_2 changed from transgranular to intergranular with Al penetration [3]. This change is an indication of grain boundary energy decrease.

The cohesive energy density calculated here is the value of energy necessary to start microcracking along the grain boundary. Experimental values were not available. Nonetheless, it is possible to make a qualitative comparison with values of TiB_2 macroscopic fracture toughness measured experimentally by Baumgartner [1]. These values show that the exposure to Al at high temperatures decreases the material fracture toughness and this corresponds to a reduction of effective fracture energy. Even though the present values refer to a specific type of cracking (i.e., microcracking along grain boundary) the model reproduces a similar reduction of cohesive energy; this was obtained by varying the Young's modulus and the failure load from experiments. Note that the measurements of K_{Ic} in Ref. [1] were carried out at $T = 960\ ^\circ\text{C}$, while in the present study the penetrated specimens were tested after cooling, at room temperature, and note also that there are differences of experimental setup and material microstructure.

Concluding remarks

Thermal mismatch induced residual stresses exert a strong influence on the grain boundary cracking in polycrystalline materials. A FE model of 4-point bending specimens was employed and cohesive elements were used to describe the damage and microcracking of a grain boundary located at the center of the specimen. Clarke's model [7] was employed to represent thermal anisotropy in a limited number of square grains, placed at the two sides of the grain boundary and surrounded by both thermally and elastically isotropic material with the average properties of TiB_2 . Even though the model makes some assumptions about grain shape and localized thermal anisotropy, it is believed to be appropriate for a preliminary analysis of the local thermal anisotropy effect on grain boundary microcracking initiation. Clarke's model was employed previously to model the strengthening effect of nanoparticles on ceramic composites [18].

It was found that the failure strength is strongly affected by the presence of thermal mismatch induced residual stresses. For microstructures with grain size $10\ \mu\text{m}$, the failure strength at $G_c = 0.01\ \text{N/mm}$ was found to be about 4 times larger than the case without residual stresses. Furthermore, when the grain boundary energy is large the residual stress effect on microcracking initiation tends to vanish. The numerical results show that grain size and grain orientation as well as number of grains play a significant role in the residual stress distribution.

It should be noted that simple square grain shape has been applied in this study. A discussion about the effect of grain shape on the residual stress distribution and microcracking susceptibility can be found in [4]. Evans [4] studied a single hexagonal grain configuration first and focused on the grain facet normal to the direction of maximum expansion. It was concluded that the relaxation of the other boundaries generates an increase of the stress singularity term at the extremities of the facet of interest. In addition, it was found that the hexagonal grain shape is the one that corresponds to the worst scenario for the microcracking from triple point defects of the single grain configuration. In a multigrain configuration, the effect of the neighboring grains is to increase the stress all along the facet under study, not just the stress singularities at the extremities. Note that the relative grain orientations play an important role: neighboring grains with similar orientations maximize the stress on the facet under study. In the present case, the use of square grains implies a different stress distribution along the facet of interest; but the resultant stress is largely dependent on the relative grain orientations of neighboring grains. Therefore, we can conclude that the present results are probably a slight underestimate of the stress fields of hexagonal multigrain configurations.

Variations of the employed critical traction of ± 100 MPa, has a small effect on the failure strength. In particular the effect of the critical traction on the failure strength is almost negligible in the case with residual stresses. For what concerns the interface stiffness, the bound values are identified in order to overcome numerical problems.

The experimental failure loads measured in our previous study [3], for both pristine and aluminum-infiltrated TiB_2 , were used to identify the corresponding grain boundary energy from the simulations with residual stresses. It was concluded that a cohesive energy density of about 0.025 N/mm corresponds to the experimental failure load 579 N (flexural strength 300 MPa), assuming $\sigma^0 = 800$ MPa. The presence of liquid Al decreases the grain boundary energy.

During the simulation of the microcracking of the brittle interface by cohesive elements, convergence problems

occurred, especially in the case without residual stresses. The introduction of a small fictitious viscosity in the cohesive law in combination with the use of a small-step increment in the simulations, improved the convergence rate and the effect on the results (microcracking initiation) is negligible.

Acknowledgement This study is part of the research project (2003–2008) ThermoTech (Thermodynamics Applied to High Temperature Materials Technology) at the Norwegian University of Science and Technology (NTNU), Trondheim.

References

1. Baumgartner HR (1984) *J Am Ceram Soc* 67:490
2. Pettersen G (1997) Development of microstructure during sintering and aluminum exposure to titanium diboride ceramics. PhD Thesis, NTNU, Trondheim, NO
3. Jensen M, Pezzotta M, Zhang ZL, Einarsrud M-A, Grande T (2008) *J Eur Ceram Soc* 28:3155
4. Evans AG (1978) *Acta Metall* 26:1845
5. Fu Y, Evans AG (1985) *Acta Metall* 33:1515
6. Laws N, Lee JC (1989) *J Mech Phys Solids* 37:603
7. Clarke DR (1980) *Acta Metall* 28:913
8. Pezzotta M, Zhang ZL, Jensen M, Grande T, Einarsrud M-A (2008) *Comput Mater Sci* 43:440
9. Turon A, Davila CG, Camanho PP, Costa J (2007) *Eng Fract Mech* 74:1665
10. Alfano G, Crisfield MA (2001) *Int J Numer Methods Eng* 50:1701
11. Chaboche JL, Feyel F, Monerie Y (2001) *Int J Solids Struct* 38:3127
12. Gao YF, Bower AF (2004) *Modell Simul Mater Sci Eng* 12:453
13. Samimi M, van Hal BAE, Peerlings RHJ, van Dommelen JAW, Geers MGD (2007) An enriched cohesive zone model for numerical simulation of interfacial delamination in Microsystems. In: International conference on thermal, mechanical and multi-physics simulation experiments in microelectronics and microsystems, EuroSime2007, 16–18 April, London, UK
14. Munro RG (2000) *J Res Natl Stand Technol* 105:709
15. ABAQUS (2006) User's analysis manual, version 6.6
16. Hilleborg A, Modeer M, Petersson PE (1976) *Cem Concr Res* 6:773
17. Hu X, Duan K (2008) *Int J Fract* 154:3
18. Kovalev S, Ohji T, Yamauchi Y, Sakai M (2000) *J Mater Sci* 35:1405. doi:10.1023/A:1004758831048